Infrared spectroscopic confirmation of z~2 photometrically selected obscured quasars

Ishikawa, Y.; Wang, B.; Zakamska, N.L.; Richards, G.T.; Hennawi, J.F.; Rivera, A.B.

Infrared spectroscopic confirmation of $z \sim 2$ photometrically selected obscured quasars

Yuzo Ishikawa [1]★ Ben Wang,[2,3] Nadia L. Zakamska [1,4] Gordon T. Richards,[5] Joseph F. Hennawi [3,6] and Angelica B. Rivera[7]

[1]*Department of Physics and Astronomy, Bloomberg Center, Johns Hopkins University, Baltimore, MD 21218, USA*
[2]*Department of Astronomy, Tsinghua University, Beijing 100084, China*
[3]*Leiden Observatory, Leiden University, P.O. Box 9513, NL-2300 RA Leiden, The Netherlands*
[4]*Institute for Advanced Study, Princeton University, Princeton, NJ 08544, USA*
[5]*Department of Physics, Drexel University, 32 S. 32nd Street, Philadelphia, PA 19104, USA*
[6]*Department of Physics, Broida Hall, UC Santa Barbara, Santa Barbara, CA 93106-9530, USA*
[7]*Department of Physics, US Naval Academy, 572C Holloway Rd., Annapolis, MD 21402, USA*

ABSTRACT

The census of obscured quasar populations is incomplete and remains a major unsolved problem, especially at higher redshifts, where we expect a greater density of galaxy formation and quasar activity. We present Gemini GNIRS near-infrared spectroscopy of 24 luminous obscured quasar candidates from the Sloan Digital Sky Survey's Stripe 82 region. The targets were photometrically selected using a *WISE*/W4 selection technique that is optimized to identify IR-bright and heavily reddened/optically obscured targets at $z > 1$. We detect emission lines of Hα, Hβ, and/or [O III] in 23 sources allowing us to measure spectroscopic redshifts in the range $1 < z < 3$ with bolometric luminosities spanning $L = 10^{46.3}$–$10^{47.3}$ erg s^{-1}. We observe broad 10^3–10^4 km s^{-1} Balmer emissions with large Hα/Hβ ratios, and we directly observe a heavily reddened rest-frame optical continuum in several sources, suggesting high extinction ($A_V \sim 7$–20 mag). Our observations demonstrate that such optical/infrared photometric selection successfully recovers high-redshift obscured quasars. The successful identification of previously undetected red, obscured high-redshift quasar candidates suggests that there are more obscured quasars yet to be discovered.

Key words: galaxies: high-redshift – quasars: emission lines – quasars: general – quasars: supermassive black holes – infrared: galaxies.

1 INTRODUCTION

According to the standard unification model, many of the observed properties of active galactic nuclei (AGN) may be explained by differences in the viewing angle with respect to the dusty torus (e.g. Antonucci 1993). In this scheme, there is a compact source of optical, ultraviolet (UV) and X-ray emitting continuum associated with the accretion disk and the corona near the supermassive black hole. On larger scales, other components include the broad-line region, the dusty obscuring torus, and the narrow-line region of gas photoionized by the quasar radiation (e.g. Krolik & Begelman 1988; Lawrence & Elvis 2010). In this picture, Type-1 quasars are observed with a direct line of sight to the central source revealing the broad emission lines. Type-2 quasars are observed sideways through the obscuring torus, so that only narrow (and forbidden) emission lines and infrared (IR) emission produced by the reprocessing in the torus are observed.

In addition to the purely orientation-based hypothesis for the difference between obscured and unobscured sources, there are other possible interpretations. Popular galaxy evolution models postulate that unobscured and obscured quasars represent different phases of evolution. In this picture, the obscured phase precipitates a phase of strong mechanical feedback, during which the obscuring material is expelled to reveal the unobscured quasar (e.g. Sanders et al. 1988; Canalizo & Stockton 2001; Hopkins et al. 2006; Glikman et al. 2012). There is evidence that some obscured sources, although a minority, may be caused by transient absorbers in the line of sight (e.g. LaMassa et al. 2015). Some of the most luminous obscured quasars at high redshifts like extremely red quasars (ERQs) may be super-Eddington accretors (e.g. Assef et al. 2015; Perrotta et al. 2019; Zakamska et al. 2019). These quasars may be obscured by inflowing and outflowing materials. Quantifying and characterizing obscured quasars remains an ongoing problem in modern astrophysics.

A complete understanding of the growth of supermassive black holes requires a complete census of both the unobscured and obscured quasar populations. The unification models predict that the number density of unobscured and obscured quasars should be comparable through cosmic time, peaking at $z \sim 2.5$ (Richards et al. 2006; Ross et al. 2013). A large population of obscured quasars would affect our existing calculations of the accretion efficiency of supermassive black holes (Soltan 1982; Yu & Tremaine 2002). Furthermore, obscured quasars are a key component to the cosmic X-ray background (e.g. Treister & Urry 2005; Lanzuisi et al. 2009). Moreover, $z \sim 2$ marks the epoch of rapid growth of the supermassive black holes through

★ E-mail: yishika2@jhu.edu

mass accretion in the most luminous quasars, so it is critical to characterize the quasars at high redshift.

Decades of work have established that the number density of unobscured and obscured quasars at low redshifts ($z < 1$) are comparable (Reyes et al. 2008; Lawrence & Elvis 2010). However, the census at high redshift remains incomplete and debated (e.g. Polletta et al. 2008; Eisenhardt et al. 2012; Hennawi & Prochaska 2013; Lusso et al. 2013; Prochaska et al. 2013; Assef et al. 2015). Some X-ray studies suggest that the obscured fraction may be a function of luminosity with an anti-correlation between obscured fraction and quasar luminosity, yet remain debated (e.g. Ueda et al. 2003; Glikman et al. 2018). The apparent paucity may imply that obscured quasars are not very common, possibly due to physical changes in their obscuring medium (Lawrence 1991; Konigl & Kartje 1994; Elitzur & Shlosman 2006; Hasinger 2008). Alternatively, they may have eluded discovery due to incomplete selection. It is important to highlight the difficulty of observing obscured quasars. Quasars typically outshine their host galaxies by several orders of magnitude in the rest-frame UV and optical wavelengths. However, a key characteristic of obscured quasars is that dust obscuration in the line of sight can heavily redden the quasar continuum. As a result, the largest catalogues of obscured quasars are largely limited to low redshift targets that are optically selected based on their extremely strong narrow emission lines that originate outside of the obscuring material (e.g. Zakamska et al. 2003; Reyes et al. 2008; Yuan, Strauss & Zakamska 2016). Alternatively, powerful X-ray detections can be indicative of quasar activity. However, the X-ray selection is typically limited to sources with modest column densities that allow hard X-rays to travel unimpeded. At extremely high, Compton-thick column densities, the absorption makes X-ray detections prohibitively difficult, despite high intrinsic luminosities of the quasar hidden behind the obscuration (e.g. Goulding et al. 2018; Zappacosta et al. 2018; LaMassa et al. 2019; Ishikawa et al. 2021). Therefore, a more robust strategy is to take advantage of the dust obscuration by probing the mid-infrared (MIR) emission, which is thought to be both more universal and isotropic, compared to UV/optical selections. Even Compton-thick quasars should be MIR-bright due to the reprocessed emission from the warm/hot dust in/around the obscuring torus. However, caution is needed as this method has many contaminants. For example, MIR continuum emission can also result from intense star-forming galaxies; the clumpy nature of the torus, which can allow MIR emission to escape unimpeded; and dust in the polar regions rather than the obscuring torus (Hickox & Alexander 2018).

MIR-based colour selection using *WISE* (Wright et al. 2010) or *Spitzer* (Werner et al. 2004) has had successes in identifying obscured quasars. Recent work (Eisenhardt et al. 2012; Wu et al. 2012; Yan et al. 2013; Ross et al. 2015; Glikman et al. 2018) demonstrated that a combined selection of bright mid-IR sources that are optically faint efficiently identifies obscured quasars both at $z < 1$ and at $z \sim 2$. However, canonical mid-IR *Spitzer*/IRAC colour selection wedges, which rely on 8μm (rest-frame 2.7μm) fluxes, do not sufficiently probe the peak of the quasar-heated dust emission at ~ 10μm (Lacy et al. 2004; Stern et al. 2005; Polletta et al. 2008; Donley et al. 2012; Lacy et al. 2013) and may miss populations of high redshift obscured quasars. Therefore, it would be ideal to probe even longer wavelengths, such as with the all-sky *WISE*/W4 (~ 22μm) coverage, complemented with *Spitzer* observations. In this paper, we take advantage of colour-selection strategies based on both *WISE*/W4 and *Spitzer* fluxes to select luminous $z \sim 2$ obscured candidates over an area larger than those of the previous searches. This paper is structured as follows. In Section 2, we

discuss the sample selection and data reduction. In Section 3, we present the analysis of spectra and photometry of our candidates. In Section 4, we discuss the implications of our results, and we conclude in Section 5. We use the AB magnitude system unless otherwise specified. We adopt the $h = 0.7$, $\Omega_M = 0.3$, and $\Omega_\Lambda = 0.7$ cosmology.

2 TARGET SELECTION

2.1 Sample selection

Our selection uses *WISE*, *Spitzer*, and Sloan Digital Sky Survey (SDSS) data to identify sources that are MIR luminous, yet optically faint. First, *WISE*/W4 bright sources are selected. We require 5σ detection with $6 < W4 < 8$ Vega mag ($f_{W4} \geq 5$ mJy). The bright limit is applied to reduce stellar contamination. Additional criteria are applied to ensure robust MIR detections and to limit contamination from stars and other spurious sources: 5σ detection of *WISE*/W3 (~ 12μm) and $W1 \geq 12$ Vega mag. We also consider the *WISE* data-quality flags to avoid artefacts (w4flg = 0 and w3flg = 0) and to limit to point-sources (ext_flg = 0 and nb ≤ 2). These *WISE*-selected sources are then cross-matched with *Spitzer* surveys to obtain precise astrometry of ∼0.1 arcsec for narrow-slit spectroscopic follow-up.

The MIR selections are further narrowed down to identify optically faint sources. The full search area includes fields from SHELA (Papovich et al. 2016), SWIRE (Lonsdale et al. 2003), SERVS (Mauduit et al. 2012), COSMOS (Sanders et al. 2007), SDWFS, and AllWISE surveys. For this *Gemini*/GNIRS study, we limit the selection to optically faint sources from the *Spitzer* IRAC Equatorial Survey (SpIES; PI Richards), which is a SWIRE-depth survey in the SDSS Stripe 82 area (Timlin et al. 2016). Stripe 82 is the largest field considered. The effective search area is $\gtrsim 164$ deg^2. We define optical faintness as either having $r > 23$ AB mag or undetected in the SDSS (York et al. 2000). If we combine the SDSS and *WISE* + *Spitzer* selections, we obtain a $r - W4 > 13.5$ colour cut. The effective colour cut implied by these criteria is somewhat more stringent than that for the selection of Dust Obscured Galaxies (DOGS; Dey et al. 2008). Previous studies (Brand et al. 2007; Ross et al. 2015) show that this selection uncovers luminous obscured quasars at $z \sim 2$. We identified 373 sources from the W4 selection over all fields considered. This selection recovers 15 known $z < 1$ sources and 22 known $z > 1$ sources, of which 18 are known $z > 1$ Type-2 or reddened Type-1 quasars, including a $z = 3.106$ HotDOG (Glikman et al. 2013; Lacy et al. 2013; Banerji et al. 2015; Tsai et al. 2015; Glikman et al. 2018). From the candidates, we selected sources that lack spectroscopic confirmation. We find 26 optically faint sources in the Stripe 82 region that are appropriate for *Gemini*/GNIRS. Interestingly, only three sources are detected in SDSS photometry. We obtained *Gemini*/GNIRS spectra for 24 of these sources to identify the Hα emission line to obtain spectroscopic redshifts.

In Fig. 1 we show a colour–colour plot of the sources to compare with other known colour-selected obscured quasars. We stress that our selections do not rely on $W1 - W2$ or $W1 - W4$ colours. We discuss the implications of the selection criteria in Section 4.1. We list our *Gemini*/GNIRS-observed targets and their selection properties in Table 1. We summarize the selection criteria here:

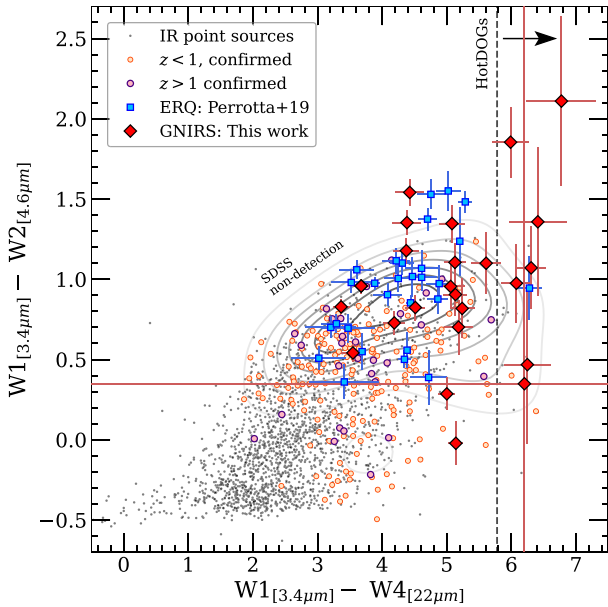$W4 \geq 5$ mJy

$r > 23$, or undetected in SDSS.   (1)

Figure 1. The colour–colour distribution of the *WISE*/W4 selected objects. The black points show the distribution of $f_{24\mu m} > 1$ mJy point sources detected in *Spitzer*/IRAC. The orange and purple circles indicate spectroscopically confirmed $z < 1$ and $z > 1$ sources, respectively. The grey contours indicate the SDSS non-detections. The red diamonds indicate our sources. We stress that our selections in this study primarily rely on *WISE*/W4 and SDSS fluxes. Any suggestive colour–colour relations may serve as a guide for future searches of obscured quasars. We also compare with the colour cuts of HotDOGs (Eisenhardt et al. 2012; black dashed line) and the observed *WISE* colours of ERQs (Perrotta et al. 2019; blue squares): both of which rely on colour-based selections.

2.2 Observation and reduction

The targets were observed with the *Gemini*/GNIRS spectrograph (Elias et al. 2006a, b) under GN-2017B-Q-51 (PI: Richards) over several nights spanning 2017 September 27 to 2018 January 03. We used GNIRS with the 0.15 arcsec/pixel camera and the 32 l/mm grating in the cross dispersed mode for a coverage over 0.9–2.4 µm. We used the 0.45 arcsec slit for an effective spectral resolution of $R \sim 1100$. Observations were performed with the ABBA observing sequence. Each object has a total integration time of 2400s. We reduce the data with the PYPEIT pipeline (Prochaska et al. 2020a, b). This reduction produces fully calibrated science spectra. For objects with clear continuum, we run the automatic spectra extraction routine. For objects with faint or no continuum detected, we manually look for emission lines to select the extraction aperture in the 2D spectra for the spectral extraction. Flux calibration is applied with standard stars observed on the same night. Telluric corrections are also applied.

We examine the fully reduced and calibrated spectra to categorize the sources as A/B/C/D based on the observed continuum and emission line strengths. The sources are classified into the following categories: (A) strong line(s) with strong continuum, (B) weak line(s) with weak continuum, (BB) 'B'-type with a blue-sloped excess, (C) weak line with no continuum, and (D) no line and no continuum. We indicate these classifications in Table 1. We are able to confidently categorize most sources, although some required additional Keck/LRIS observations for confirmation (Wang et al., in prep).Roughly half of the observed sources have significant emission lines and/or continuum. The other half show emission with low equivalent widths, which made it difficult to determine the

spectroscopic redshift. Only one source (J0047+0003) showed no features. We show a subset of the observed sources with significant emission and/or continuum in Fig. 2.

3 RESULTS: SPECTRAL ANALYSIS

3.1 Redshift estimates

We compute the redshifts in two steps. First, we visually identify emission lines of interest (e.g. Hα and Hβ+[O III]) to determine the rough spectroscopic redshift. We set these as priors to fit Gaussians to the observed emission lines. We then refine the spectroscopic redshift with the best-fitting line centroid shifts. To this end, we first subtract out the underlying continuum. All sources with strongly detected continuum flux have a red slope. We define the continuum by masking out the emission lines and telluric contamination at $\sim 1.4\mu m$ and $\sim 1.9\mu m$ and interpolating over the masked spectrum. Finally, we fit single Gaussians to the continuum-subtracted emission line spectrum.

For targets with sufficient GNIRS detections, we take the Hα and/or Hβ+[O III] lines to estimate the spectroscopic redshifts. The observed equivalent widths of the emission lines vary. For sources with heavy telluric contamination, we use other emission lines for spectroscopic redshift determination. For example, J0213+0024 and J2243+0017 show heavy $\sim 1.9\mu m$ telluric contamination, making it difficult to accurately find the centroid of the Hα line; instead we use the [O III] doublet and [O I]λ8446Å. If we only detect one emission line (e.g. J2334 + 0031), then we assume it is Hα. We fit the [O III] doublet by kinematically tying the lines to [O III]5009Å and setting the peak flux [O III] line ratio λ5009Å/λ4959Å = 2.993. Some sources were originally identified as featureless 'D'-sources, but were confirmed with Keck/LRIS observations (Wang et al., in prep). For example, the Hα line for J0112−0016 is redshifted out of the GNIRS coverage, and the one line visible in the GNIRS spectrum turns out to be [O III]. In Table 2, we show the redshift estimates from *Gemini*/GNIRS-only data, z_{GNIRS}, and the 'best' estimates from the combined *Gemini*/GNIRS+Keck/LRIS data, z_{best}. The differences in the redshift estimates highlight how challenging it can be to identify obscured quasars. In Fig. 3, we show the redshift distribution of the spectroscopically confirmed objects. We can see that the initial colour selection preferentially selects $1 < z < 3$ objects with the average redshift of $\langle z_{best} \rangle = 2.008 \pm 0.45$. We do not see any redshift dependence on the spectral types outlined in Section 2.2.

3.2 Emission line properties

After we obtain the best-fitting line parameters, we calculate the line luminosities. The line luminosity is calculated as the observed fluxes multiplied by $4\pi D_L^2$ assuming that the emission is isotropic, where D_L is the luminosity distance at z_{best}. In Table 2, we show the calculated line luminosity and the full-width-half-maximum (FWHM; 2.355σ). The Hα line is the brightest with luminosity reaching 10^{42}–$10^{43.4}$ erg s^{-1}, whereas the Hβ+[O III] lines are nearly $\times 10$ fainter. The observed Hα fluxes are commensurate with those of DOGS (Brand et al. 2007). This is also at the limit of GNIRS sensitivities, based on GNIRS ITC predictions of emission from a $z = 2.3$ source with 1×10^{-16} erg s^{-1} cm^{-2} and FWHM $\times$ 1000 km s^{-1} superposed on a continuum of 1×10^{-18} erg s^{-1} cm^{-2}Å^{-1}.

In Fig. 4, we show the relationship between emission line widths (FWHM) and luminosities. We find no obvious correlations between

Table 1. Sample list of observed quasars. The target coordinates are determined from *Spitzer* + *WISE* and SDSS photometry. The targets are ordered by coordinates. Sources observed on different dates have been co-added to produce a single spectrum. We list the selection properties. We classify the sources as A/B/BB/C/D based on their continuum and emission line strengths. All continuum detections have a red slope; 'BB' marks sources with a blue excess. † denotes sources with no SDSS detections; SDSS r-band upper limit is $r > 23$ AB mag (York et al. 2000).

Target name	RA (J2000)	DEC (J2000)	Date(s) observed (yyyy-mm-dd)	W4 [22μm] (AB mag)	r'_{SDSS} (AB mag)	Category
J002407.02−001237.2	00:24:07.02	−00:12:37.2	2017 October 06	7.39 ± 0.12	$-^†$	C
J004157.77−002932.1	00:41:57.77	−00:29:32.1	2017 October 07	7.94 ± 0.21	$-^†$	BB
J004729.25+000358.8	00:47:29.25	+00:03:58.8	2017 October 21, 2017 October 30	7.67 ± 0.16	$-^†$	D
J005424.45+004750.2	00:54:24.45	+00:47:50.2	2017 October 21	7.21 ± 0.13	$-^†$	C
J010552.86−002351.2	01:05:52.86	−00:23:51.2	2017 October 21, 2017 October 30	7.78 ± 0.16	$-^†$	C
J011222.64−001633.0	01:12:22.64	−00:16:33.0	2017 November 05	7.73 ± 0.20	$-^†$	C
J011314.49+002917.1	01:13:14.49	+00:29:17.1	2017 November 05	7.85 ± 0.19	$-^†$	C
J013033.47+000950.4	01:30:33.47	+00:09:50.4	2017 November 05	7.98 ± 0.20	$-^†$	C
J014939.96+005256.7	01:49:39.96	+00:52:56.7	2017 November 07	7.95 ± 0.17	$-^†$	B
J015055.28+005600.2	01:50:55.28	+00:56:00.2	2017 November 06	7.98 ± 0.21	$-^†$	D
J015235.29−002459.4	01:52:35.29	−00:24:59.4	2017 November 06	7.26 ± 0.09	22.57 ± 0.18	A
J021345.44+002436.1	02:13:45.44	+00:24:36.1	2017 November 07	7.86 ± 0.16	$-^†$	A
J021426.98−000021.3	02:14:26.98	−00:00:21.3	2017 November 07, 2017 November 09	7.56 ± 0.12	$-^†$	C
J021514.76+004223.8	02:15:14.76	+00:42:23.8	2017 September 27	7.39 ± 0.12	$-^†$	B
J022127.60+005024.6	02:21:27.60	+00:50:24.6	2017 September 29	7.70 ± 0.14	$-^†$	C
J222920.83+002253.5	22:29:20.83	+00:22:53.5	2017 November 07	7.04 ± 0.11	$-^†$	C
J223358.38−000414.9	22:33:58.38	−00:04:14.9	2017 November 05	7.81 ± 0.19	$-^†$	D
J223904.01−003054.9	22:39:04.01	−00:30:54.9	2018 January 02	7.46 ± 0.16	$-^†$	D
J223911.98−005422.3	22:39:11.98	−00:54:22.3	2017 September 29, 2017 September 30	7.75 ± 0.18	23.31 ± 0.32	D
J224338.04+001749.9	22:43:38.04	+00:17:49.9	2017 September 30	7.51 ± 0.17	$-^†$	A
J225851.90−002207.0	22:58:51.90	−00:22:07.0	2017 October 01	7.89 ± 0.20	$-^†$	C
J225956.84−000918.4	22:59:56.84	−00:09:18.4	2018 January 03	7.76 ± 0.19	$-^†$	B
J232925.01+002057.7	23:29:25.01	+00:20:57.7	2017 November 07	7.88 ± 0.19	$-^†$	C
J233441.49+003114.0	23:34:41.49	+00:31:14.0	2017 November 06	7.62 ± 0.16	23.10 ± 0.22	BB

the line width and the line luminosity. We further see that the Hα emission lines consistently show broad profiles with FWHM of several 1000 km s^{-1}. In contrast, the [O III] width distribution is concentrated around FWHM = 1000–3000 km s^{-1}. For the nine sources with both Hα and [O III] detections, the Kolmogorov–Smirnov (KS) test does not indicate a strong correlation between the line widths. This lack of correlation may suggest that the observed Hα and [O III] kinematics may originate from different mechanisms (e.g. BLR and NLR emission versus outflows). To better understand the observed line kinematics, we compare our [O III] measurements with those of other quasar samples: $z < 1$ Type 2 (Zakamska & Greene 2014), $z \sim 2$ Type 2 (Harrison et al. 2012), $1.5 < z < 3.5$ Type 1 (Shen 2016), $2.3 \lesssim z \lesssim 3.5$ quasars (Bischetti et al. 2017), and $z \sim 2$ ERQs (Perrotta et al. 2019). We can see that the [O III] emission lines in our sample are much fainter, yet are broad. The observed line properties are mostly consistent with other known Type-2 quasars. Zakamska & Greene (2014) show median [O III] FWHM of ∼890 km s^{-1}, ranging between 340 and 4390 km s^{-1}, after converting from w_{80}.

In addition to Hα, we see various low-ionization lines like [O I]λ6300Å and [O II]λ3727Å in certain sources (e.g. J0213+0024, J2243+0017, J0149+0052, J0215+0042). [O I] may be suggestive of shocks or outflows in the neutral medium. The non-detection of Fe II further supports that these targets are indeed obscured or red quasars. The focus of this paper will be on the Hα and Hβ+[O III] lines.

3.3 Rest-frame optical versus IR

Due to the nature of the colour selection, all our targets have strong IR fluxes, despite variations in the optical emission. We compare the monochromatic IR luminosity at rest-frame $\lambda = 5$μm, which we denote as $L_{5μm} \equiv \lambda L_\lambda(5μm)$. Since the observed broadband *WISE* filters correspond to different rest-frame wavelengths, we must interpolate over the observed *WISE* fluxes, $F_{\lambda, obs}$. We assume the IR spectra take a power-law form $L_\lambda \propto \lambda^\alpha$ and interpolate to compute $L_{5μm}$. We find an average slope of $\langle \alpha \rangle = 1.05 \pm 0.6$ around 5μm. All sources are very IR luminous with $L_{5μm} \sim 10^{46} - 10^{47}$erg s^{-1}, comparable to the brightest known obscured quasars (e.g. Ross et al. 2015). We also calculate the bolometric luminosity by using the IR-bolometric correction $L_{bol} = 8 \times L_{3.45μm}$ (Hamann et al. 2017; Perrotta et al. 2019). We denote $L_{3.45μm}$ as the monochromatic luminosity at $\lambda = 3.45$μm, which is extrapolated from the computed $L_{5μm}$ value using the same piece-wise power-law interpolation described above. L_{bol} reaches and exceeds 10^{47}erg s^{-1}. We list the calculated $L_{5μm}$ and L_{bol} values in Table 2. We calculate the source luminosities (emission line and bolometric) assuming isotropic emission. This assumption means that if obscuration makes the observed IR emission anisotropic, as is the case with low redshift Type-2 quasars (Liu et al. 2013), then the actual L_{bol} may even be higher as noted by Zakamska & Greene (2014).

In Fig. 5, we show the Hα and [O III] line luminosities and kinematics, along with with the computed $L_{5μm}$, which we use
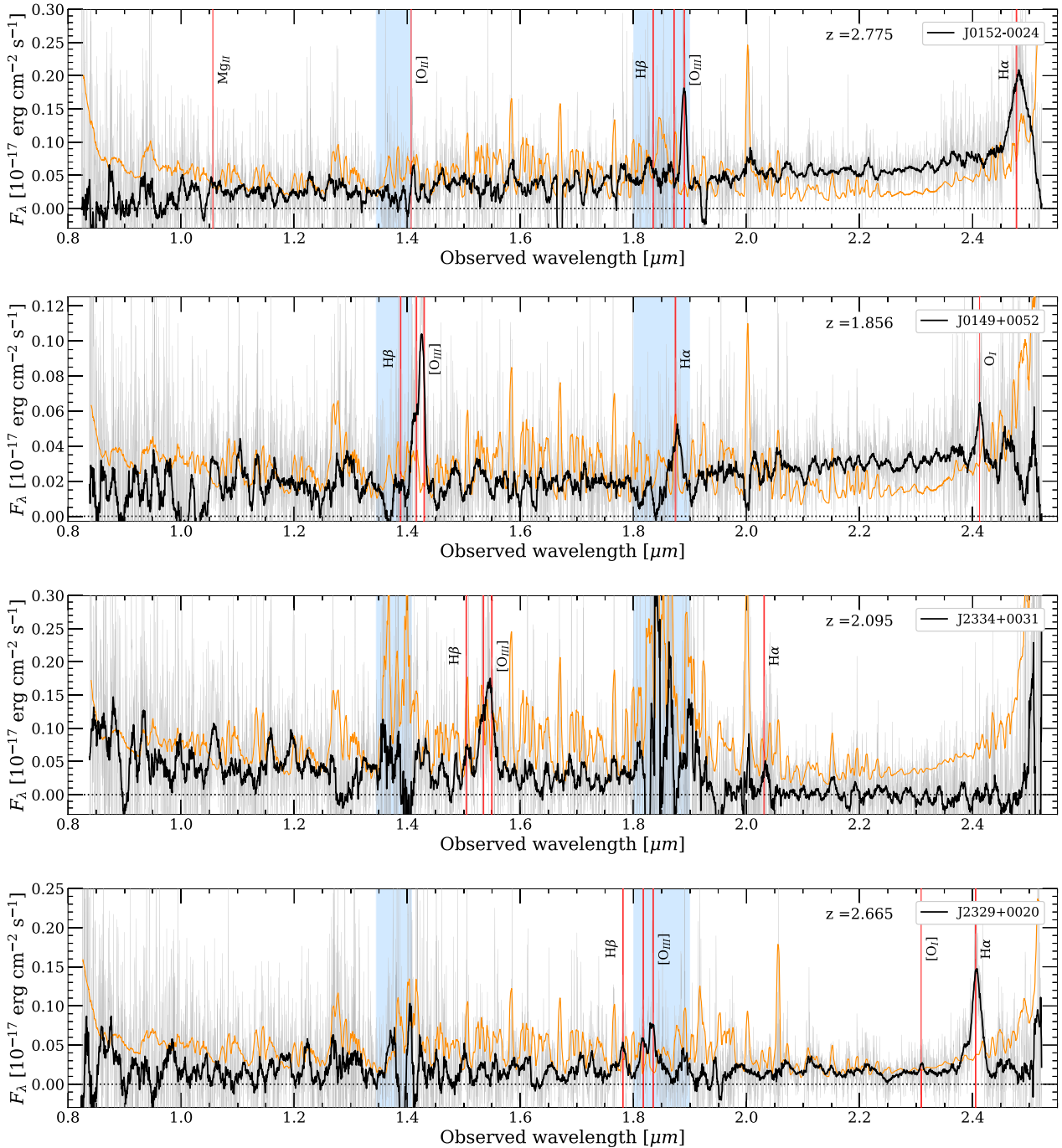
Figure 2. Example spectra of A/B/BB/C sources with continuum and/or emission lines detected. We do not show the featureless D-sources here. The shaded blue regions mark telluric absorption, and the orange curve is the noise vector plot. Raw spectra are in light grey and the smoothed spectra in bold black. The vertical red lines indicate the emission lines identified.

as a proxy for L_{bol}. We do not see any obvious correlations between the Hα and [O III] line kinematics and $L_{5\mu m}$.

3.4 Spectral energy distribution (SED) fitting

Taking advantage of the optical and IR multi-wavelength data, we construct SEDs and perform SED fits to understand the nature of our objects. In Fig. 6, we show the SEDs separated by *Gemini*/GNIRS spectral quality. Since many of the individual spectra suffer from low

SNR, we co-add the GNIRS spectra according to the A/B/BB/C/D categories defined in Section 2.2. We show the co-added spectra in Fig. 6. Interestingly, we find that the sources that did not show an obvious continuum individually now show a slight red slope after co-adding. We use the co-added spectra for the SED fits to simplify the analysis.

Based on the bright *WISE* IR emission that reaches $10^{45.5}$–10^{47}erg s^{-1}, we can assume that the SED is most likely dominated by the quasar torus emission. It is unlikely for the MIR emission

Table 2. Emission line properties of the targets listed by coordinates. * indicates sources with significant telluric absorption of $H\alpha$. † indicates sources with featureless spectra, but are spectroscopically confirmed by Keck/LRIS observations; z_{best} is the best redshift estimate, and z_{GNIRS} is the redshift estimate using only Gemini/GNIRS data. w indicate redshifts identified determined by Gemini/GNIRS and Keck/LRIS (Wang et al., in prep).

Target	z_{best}	z_G	Ref.line	$\log_{10}L_{H\alpha}$ (erg s^{-1})	FWHM$_{H\alpha}$ (km s^{-1})	$\log_{10}L_{H\beta}$ (erg s^{-1})	FWHM$_{H\beta}$ (km s^{-1})	$\log_{10}L_{[O\,III]}$ (erg s^{-1})	FWHM$_{[O\,III]}$ (km s^{-1})	$\log_{10}L_{bol}$ (erg s^{-1})
J0024−0012	1.528^w	0.925	[O III]	42.01 ± 0.06	2355 ± 193	41.5 ± 2.0	650 ± 300	42.33 ± 0.15	3300 ± 900	46.97 ± 0.02
J0041−0029	2.09^w	1.495	$H\alpha$	42.61 ± 0.01	2780 ± 1700	–	–	–	–	46.71 ± 0.05
J0047+0003	–	–	–	–	–	–	–	–	–	–
J0054+0047	2.17	2.17	$H\alpha$	–	–	–	–	–	–	47.31 ± 0.03
J0105−0023†	1.865	1.865	$H\alpha$	44.33 ± 0.05	200 ± 70	–	–	–	–	46.81 ± 0.05
J0112−0016	2.99^w	–	[O III]	–	–	–	–	41.88 ± 0.07	2000 ± 1000	47.72 ± 0.03
J0113+0029	2.33	2.33	$H\alpha$	42.38 ± 0.21	470 ± 175	–	–	–	–	46.83 ± 0.10
J0130+0009	2.5	2.5	$H\alpha$	42.70 ± 0.13	1180 ± 255	–	–	–	–	47.23 ± 0.04
J0149+0052	1.85	1.85	$H\alpha$	42.06 ± 0.09	2370 ± 450	–	–	42.43 ± 0.05	1840 ± 100	46.95 ± 0.04
J0150+0056	1.7	1.7	$H\alpha$	42.76 ± 0.39	3300 ± 1000	–	–	–	–	46.91 ± 0.04
J0152−0024	2.775	2.775	$H\alpha$	43.37 ± 0.01	3840 ± 300	–	–	42.90 ± 0.18	940 ± 100	47.35 ± 0.04
J0213+0024*	1.805	1.805	[O III]	43.05 ± 0.01	6896 ± 300	42.25 ± 0.05	5000 ± 1000	42.38 ± 0.20	2386 ± 260	47.02 ± 0.03
J0214−0000	1.627	1.627	$H\alpha$	–	–	–	–	–	–	47.03 ± 0.02
J0215+0042	0.88	0.88	$H\alpha$	42.38 ± 0.03	2150 ± 100	41.47 ± 0.39	1690 ± 1400	42.13 ± 0.12	3000 ± 200	46.27 ± 0.01
J0221+0050	2.48	2.48	$H\alpha$	42.94 ± 0.02	4400 ± 370	–	–	–	–	46.25 ± 0.04
J2229+0022	1.93	1.93	$H\alpha$	42.58 ± 0.12	2840 ± 1190	–	–	42.19 ± 0.13	950 ± 197	47.19 ± 0.03
J2233−0004†	1.602^w	–	$H\alpha$	–	–	–	–	–	–	46.23 ± 0.16
J2239−0030†	1.905^w	–	$H\alpha$	–	–	–	–	–	–	47.20 ± 0.03
J2239−0054†	2.085^w	–	$H\alpha$	–	–	–	–	–	–	47.12 ± 0.04
J2243+0017*	1.905	1.905	[O III]	–	–	–	–	44.7 ± 0.05	1865 ± 100	47.10 ± 0.04
J2258−0022	2.42	2.42	$H\alpha$	42.29 ± 0.05	2210 ± 400	–	–	–	–	46.95 ± 0.08
J2259−0009	1.885	1.885	$H\alpha$	42.09 ± 0.09	2350 ± 115	–	–	42.24 ± 0.12	1750 ± 100	47.03 ± 0.04
J2329+0020	2.665	2.665	$H\alpha$	43.18 ± 0.03	2340 ± 115	42.24 ± 0.15	677 ± 150	42.62 ± 0.11	1330 ± 280	47.16 ± 0.06
J2334+0031	2.095^w	1.355	$H\alpha$	42.19 ± 0.09	4350 ± 200	42.17 ± 0.28	1600 ± 000	42.85 ± 0.02	3500 ± 500	46.95 ± 0.06

Figure 3. Redshift distribution of the observed sources.

more luminous than ERQs, so they are unlikely to live in even more massive galaxies, as discussed in Section 4.1.

In Fig. 7, we show the different models considered. The MIR emission probed with *WISE* is consistent with a quasar+torus-dominated spectrum with a heavy reddening. We account for these observed properties by constructing an SED model consisting of: quasar (Type 1 or 2) + torus + (host galaxy, if needed) with varying dust absorption. We use the SWIRE galaxy and quasar spectral templates (Polletta et al. 2007). We do not include the SDSS upper limits since they are too shallow to be constraining. Here, we determine the best SED (quasar/host/torus emission strength) and the estimated A_V continuum reddening.

We assume a 'cold screen of dust absorption' model with an extinction. For simplicity, we use the Milky Way extinction model (Cardelli, Clayton & Mathis 1989; Calzetti et al. 2000; Gordon et al. 2003). We fit the co-added SEDs following $F_{obs} = F_{int}e^{-\tau_\lambda}$ to determine the best A_V extinction. We solve the following:

$$\log F_{obs} = \log k_1 F(QSO+torus+gal) - k_2\tau_\lambda, \qquad (2)$$

where k_1 is the normalization at 5 μm for the template quasar+torus SED and k_2 is the normalization for the extinction curve τ_λ. Initially, we attempted a simple single-phase absorption model; however, it was quickly apparent that a multicomponent absorption model is necessary (e.g. Ricci et al. 2017), to describe the red-sloped 'bump' seen with our GNIRS data. Here, we apply separate cold-dust absorption on each component (quasar, galaxy, and torus) and combine to produce a 'master' SED. Both the quasar and torus components required heavy absorption, reaching $A_V \sim 20$, whereas the galaxy component requires moderate absorption. We caution against overinterpreting the SEDs without detailed radiative transfer modelling.
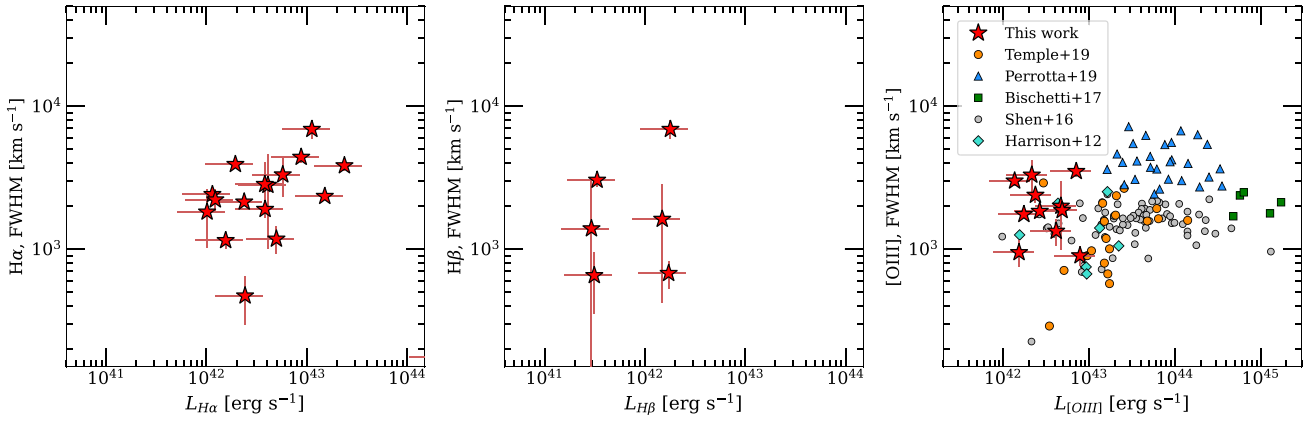
to originate from the host galaxy. For the brightest sources, if the observed light is dominated by the stellar light from the host galaxy, it would require *B* band luminosities of least $\lambda L_\lambda \sim 10^{45}$erg s^{-1} to produce $W4 \sim 10^{46}$erg s^{-1}, which is an order-of-magnitude larger than typical galaxies. For example, we know that ERQ host galaxies can be up to a few $10^{11}L_\odot \approx 10^{44.5}$erg s^{-1}. Our sources are not

Figure 4. Line kinematics and the line luminosity of Hα (left), Hβ (centre), and [O III] (right). The red symbols indicate sources with sufficient signal-to-noise ratio (SNR) for line fits. The observed Hα display broad widths similar to typical quasars. However, the width distribution of [O III] and Hα are inconsistent at ~1σ using the KS test. We also compare the [O III] properties with values from literature (Harrison et al. 2012; Zakamska & Greene 2014; Shen 2016; Bischetti et al. 2017; Perrotta et al. 2019; Temple et al. 2019). No obvious correlation between the line luminosity and widths is seen.
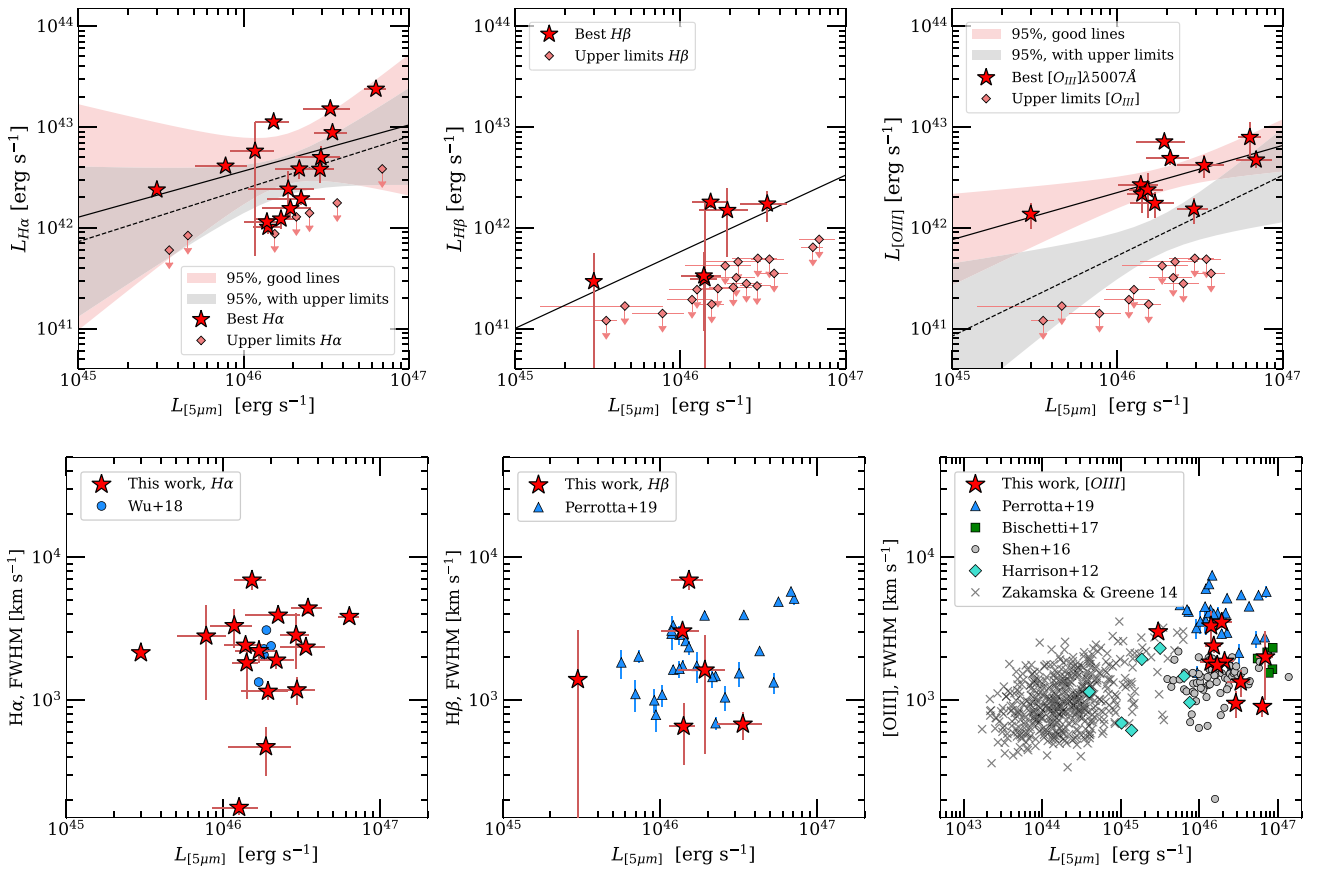
Figure 5. Line luminosities (top row) and kinematics (bottom row) shown against $L_{5\mu m}$ for Hα (left), Hβ (centre), and [O III] (right). The red symbols indicate sources with sufficient SNR for line fits. Light-red diamonds indicate the 1σ upper limits based on the average continuum flux. We also compare the Hα, Hβ, and [O III] kinematics with values from Harrison et al. (2012), Zakamska & Greene (2014), Shen (2016), Bischetti et al. (2017), Wu et al. (2018), and Perrotta et al. (2019). For the comparison with our sample, we converted the published w_{80} velocities to FWHM. Our sources show a wide range of velocities with three reaching ERQ-like velocities (see bottom right).
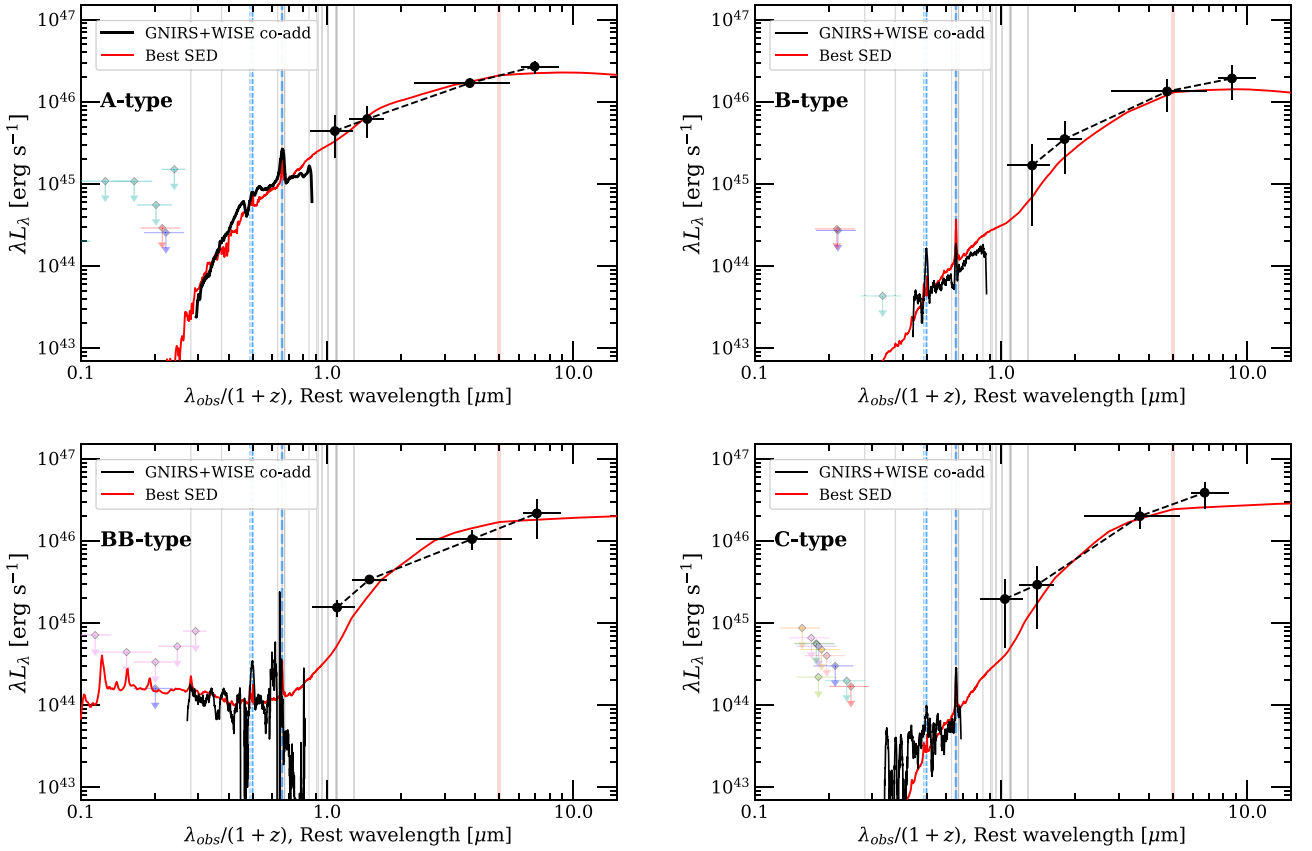
Figure 6. We show the co-added GNIRS+*WISE* SEDs overplotted in solid black line and the best-fitting SEDs in solid red line. (Top left) 'A' strong continuum and emission lines, (top right) 'B' moderate continuum and emission lines, (bottom left) 'BB' blue-sloped continuum with moderate emission lines, and (bottom right) 'C' + 'D' weak continuum with single-line Hα detection. We indicate the [O III] and Hα emission lines (light blue dashed lines), the other low-ionization lines (light grey lines), and $L_{5\mu m}$ (light red). We also plot the SDSS upper limits (light diamonds).
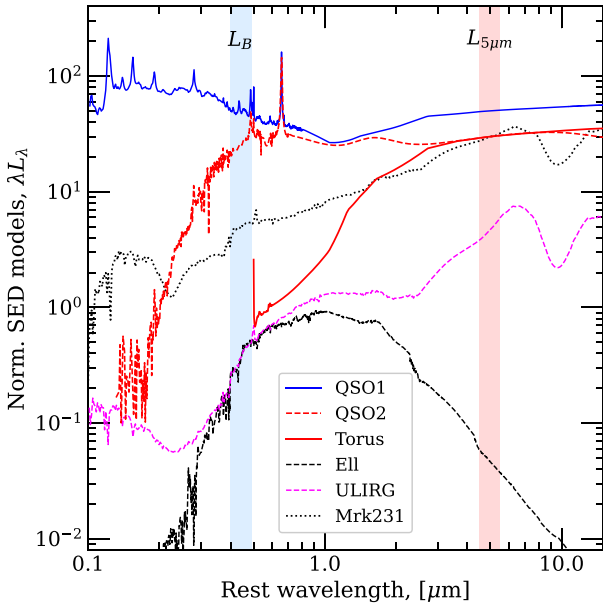
Figure 7. The model SEDs from SWIRE (Polletta et al. 2007). The plots are normalized by $\lambda L_\lambda \sim 10^{45}$ erg s^{-1}. The galaxy models are scaled at $L_B \sim 10^{44.5}$ erg s^{-1}, and the quasar models are scaled at $L_{5\mu m} \sim 10^{46.3}$ erg s^{-1}.

In Fig. 6, we show the best SED fits. As expected, we find that the *WISE*-detected MIR emission is best fit with a torus model. The GNIRS-detected rest-frame optical spectra are best fit with a quasar spectrum reddened by at least $A_V \sim 7$–20. The exception to this model is the blue excess 'BB' targets, in which an additional non-reddened quasar spectrum is needed. We explore the blue excess in Sections 4.1 and 4.3. The brightest 'A' sources require a bright galaxy component to explain the optical continuum. The exact properties of the host galaxy is unclear. What is clear is that the quasar spectrum dominates. We explore the interpretation of the reddening and the blue excess in the Discussion.

4 DISCUSSION

4.1 Efficiency of photometric selection

The redshift distribution in Fig. 3 shows that our selection preferentially selects $1 < z < 3$ objects. Unsurprisingly, the sources with stronger continuum and stronger emission lines have more reliable redshift determinations, as was noted by previous studies (e.g. Lacy et al. 2013).

Past studies of W4- and optically bright sources failed to uncover a high density of obscured quasars. In fact, the motivating colour-selection of optically faint, yet red objects, is similar to those of previous studies like ULIRGS, HotDOGs, and ERQs (i.e. $r - W4 > 14$). Instead, in this study we take a step back by considering
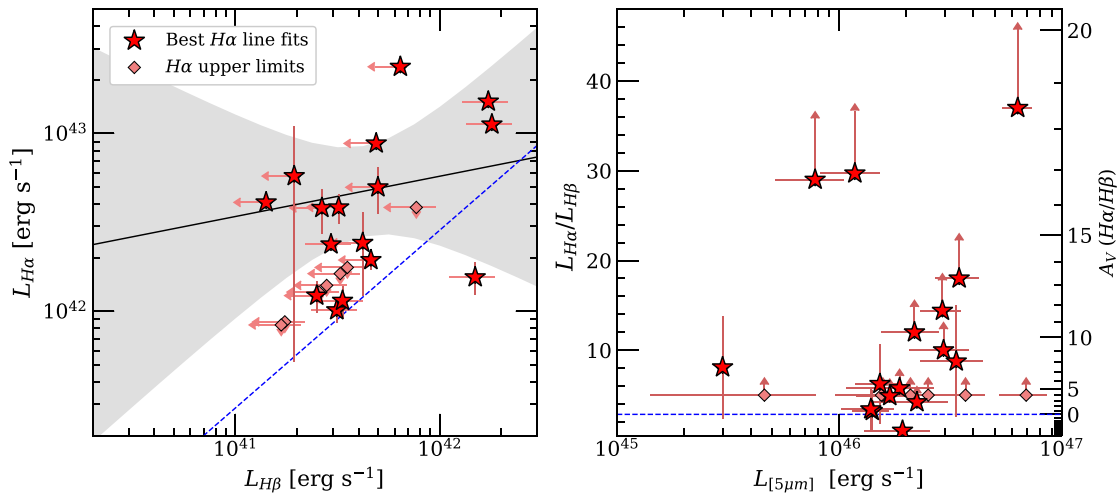
Figure 8. (Left) Luminosities of Hα and Hβ, compared with the theoretical expectation Hα/Hβ ≈ 2.9 shown with the blue dashed line. (Right) Hα/Hβ Balmer decrement shown against $L_{5\,\mu m}$. We also show the A_V calculated with Hα/Hβ. We see no obvious trends with $L_{5\,\mu m}$. Since very few sources had sufficient Hβ SNR, we place upper limits on $L_{H\beta}$, which translates to a lower bound on Hα/Hβ.

IR-bright sources with $W4 \geq 5$ mJy that have more accurate positions from *Spitzer* and that lack SDSS detections for a more robust selection.

Fig. 1 serves as a diagnostic to compare the different colour selection criteria for red and obscured quasars. The key differences in colour-selection are as follows. HotDOGs primarily rely on W1 and W2 dropouts (Eisenhardt et al. 2012): $W1 > 17.4$ Vega mag and either ($W4 < 7.7 \wedge W2 - W4 > 8.2$ Vega mag) or ($W3 < 10.6 \wedge W2 - W3 > 5.3$ Vega mag), whereas we only require bright W4 detections. ERQs are defined by $i - W4 > 4.6$ colours and [C IV] equivalent width >100Å (Hamann et al. 2017; Perrotta et al. 2019), whereas we strictly require weak *r*-band SDSS detections or non-detections in the SDSS optical photometry. Temple et al. (2019) selection of reddened quasars applied a $W1 - W2 > 0.85$ Vega mag along with *J/H/K*-band photometric cuts, which covers a redder subset of the obscured quasars discussed here. This means that our selections identifies a reddened $1 < z < 3$ population that is both HotDOG-like (but bluer) and ERQ-like (but redder), as demonstrated in Fig. 1.

Despite the similarities in the colour-selection, our sources may constitute a distinct, yet similar population to HotDOGs and ERQs. For example, only three objects record any *i*-band SDSS fluxes, which means the ERQ $i - W4$ selection would fail to identify most of our sources. All of our sources have brighter *WISE*/W4 fluxes than ERQs. Since our sources probe a bluer selection than HotDOGs, we also see a greater range in the observed rest-frame optical luminosity, with two sources showing a distinct blue excess in their spectra. The blue continuum may be indicative of scattered light. The current optically faint requirement selects against objects with a strong UV continuum, so naturally, we find very few blue-sloped targets. However, the detection of the 'BB' objects may display an analogous component to those of ERQs and Blue HotDOGs (BHDs). We explore more in Section 4.3. Failure modes of the colour-selected targets would result in either low redshift contaminants or featureless quasar spectra. However, low redshift contaminants should be minimized by limiting to optically-faint SDSS dropouts. Astrometry checks with *WISE* + *Spitzer* ensures that the *Gemini*/GNIRS pointing is robust. Barring heavy telluric contamination that prevent us from seeing the faint emission, the detection of featureless spectrum may simply reflect heavy obscuration of the inherent quasar spectrum,

whether they are at circumnuclear or galactic scales. We explore more in Section 4.2.

4.2 Levels of obscuration

As evident from the optical versus IR luminosity in Fig. 6, the quasars in our sample have substantial reddening. Here we characterize the origin of this reddening. In Fig. 8, we compare the Hα/Hβ ratio to characterize the Balmer decrement. Photoionization by the quasar is likely the dominant mechanism that gives rise to Balmer emission in our targets. The balance of photoionization and recombination sets the ratios of Balmer lines at particular values – from Case B recombination of hydrogen, the lower theoretical bound on Hα/Hβ is ≈2.98 in dust-free gas at $T_e = 10^4$ K (Dopita & Sutherland 2003; Osterbrock & Ferland 2006). Indeed, in unobscured Type-1 quasars, this value peaks at 3.3 (Kim, Ho & Im 2006). Strong enhancement in this ratio is likely due to dust extinction. We estimate A_V from the Hα/Hβ ratio following Riffel et al. (2021):

$$A_V = 7.22 \log \left(\frac{F_{H\alpha}/F_{H\beta}}{2.86} \right) \tag{3}$$

assuming an $R_V = 3.1$ extinction (Cardelli et al. 1989). Balmer decrement is typically a reliable technique to estimate dust extinction in galaxies (e.g. Kennicutt 1992). However, this may not be the case if there is no reliable measure of extinction due to the low SNR of Hβ (Assef et al. 2015; Wu et al. 2018). We see an excess of Hα of up to ~40, which translates to $A_V \sim 20$ mag. The observed Balmer decrement is consistent with the continuum reddening in Section 3.4. However, this is a little misleading since Hβ is not detected for all sources, as indicated in Table 2. Sources with significant Hβ emission have a median Balmer decrement of Hα/Hβ ~ 3.5, which correspond to $\langle A_V \rangle \sim 4.8 \pm 2.8$ mag. For sources with no Hβ detection, we indicate Hα/Hβ as lower limits. We do not see any correlation with the IR luminosity. Although we find extreme reddening in some of our sources with large Hα/Hβ values, we find that the average Hα/Hβ reddening is consistent with other Type-2 quasars. A handful show much larger Hα/Hβ than those of other known reddened quasars (e.g. Glikman et al. 2018; Jun et al. 2020). HotDOGs also show large Hα/Hβ $\gtrsim 4$ values.

We combine the cold dust extinction SED fits from Section 3.4 and the Balmer decrement estimates. From the SED fits, these sources are likely quasar-dominated, with a bright MIR component from the reprocessed emission by the torus and a significantly reddened optical component. Considering the shape of the MIR SED, which is due to warm dust, and the large continuum reddening of the intrinsic quasar spectrum, circumnuclear obscuration is the most probable scenario. Although we cannot completely rule out the possibility of galactic scale obscuration, as Temple et al. (2019) found using forbidden [O III] lines produced on large scales, our sources would nonetheless still require a circumnuclear torus to produce the observed MIR emission. While not impossible to have both circumnuclear and galactic scale obscuration, it is contrived. Our data do not have strong evidence in favour of galactic obscuration.

4.3 Properties of sources

As discussed earlier, the GNIRS observations revealed three types of sources with varying levels of continuum strengths: strong, moderate, and weak with weak lines. In Fig. 6, we show the representative SED plots. Despite differences in their rest-frame optical fluxes by up to 1.5 dexs, the IR fluxes show very similar values. The shapes of their IR SEDs are also similar. The IR luminosities reach up to $10^{46}-10^{47}$ erg s^{-1}. The best-fitting SEDs suggest that these are likely due to the quasar torus emission, suggesting the dusty nature of these quasars, complementing the non-detections in the rest-frame UV and the broad Hα and Hβ emission lines observed. These observations suggest that photometric colour selection is an excellent metric for identifying obscured quasars at $z \sim 2$.

The typical line widths of the [O III] emission in our sources are $\sim$1800 km s^{-1} at FWHM. [O III] is a forbidden emission line that must originate in low-density regions, typically well outside of the sphere of influence of the black hole. These velocity widths are too high to be contained by a realistic galaxy potential and are therefore indicative of likely galactic wind activity. However, colours alone are insufficient for identifying obscured quasars with extreme kinematics. ERQs show [O III] velocity widths in the range 1500–7400 km s^{-1} at FWHM, which are significantly higher than in the population presented here (Fig. 5, bottom right). ERQs were identified both by colours and by line diagnostics like [C IV] equivalent widths (Hamann et al. 2017; Perrotta et al. 2019; Zakamska et al. 2019). Using additional line diagnostics may be necessary to identify sources with potential quasar-driven galactic winds. We explore more in Section 4.4.

Although black hole mass scaling relations from reverberation mapping (e.g. using continuum emission and Hβ widths; Greene & Ho 2005; Vestergaard & Peterson 2006) are commonly used to estimate M_{BH}, the nature of the obscuration complicates the comparisons to obscured quasars, as noted by Zakamska et al. (2019). Supermassive black holes that are heavily obscured, have powerful winds, or are in the super-Eddington accretion limit do not necessarily obey the scaling relations because the inner broad-line region and the accretion disk are either not visible or are not in the same dynamical equilibrium as the sources used in the scaling relations. Since we have extremely low Hβ SNR and very little optical continuum, we cannot obtain reliable black hole mass measurements. With these caveats in mind, we assume that the quasars are hosted by $M_{BH} \sim 10^9 M_\odot$ black holes. This mass corresponds to an Eddington-limited ratio of $\lambda_{Edd} = L_{bol}/L_{Edd} \sim 0.7$, where $L_{Edd} \approx 1.3 \times 10^{47}$ erg s^{-1}. However, if L_{bol} is underestimated due to the obscuration, it may place these quasars closer to the Eddington limited regime. And if

the black holes are instead significantly more massive ($\sim 10^{10} M_\odot$), they may be in the accretion regime close to that of normal quasars.

Another question is the origin of the strong MIR emission. For high redshift sources, we can be confident that these are quasar dominated. However, dusty, star-forming galaxies may also produce large MIR luminosities. In Fig. 7, we compare the different SED templates, including Type-1 QSO, Type-2 QSO, Torus, Starbursts, and ULIRGs. Fortunately, dusty star-forming galaxies like ULIRGs typically have cooler SEDs compared to the quasar torus emission. Also, considering the extreme optical faintness of our objects, it is unlikely to simultaneously produce high IR emission with low optical emission. As explored in Section 3.4, a more likely scenario is dominant torus emission with a faint host galaxy with $L_B \sim 10^{44.5}$ erg s^{-1} with extreme reddening of the UV/optical quasar spectrum. There are curious 'BB' sources like J2334+0031 and J0041−0029 that display a noticeable blue continuum. These two sources also recorded SDSS fluxes at the survey's limiting magnitude, which is consistent with a UV quasar spectrum (Fig. 6). A blue excess in obscured quasars is observed when light from the quasar continuum is scattered off the surrounding gas into our line of sight. This phenomenon has been directly confirmed in ERQs with spectropolarimetric observations (Alexandroff et al. 2018). Zakamska et al. (2006), Alexandroff et al. (2018), and Assef et al. (2022) have shown that polarization and blue excess reveal scattering from dust within the ionization cone. Assef et al. (2016, 2022) also identified a subset of the HotDOG population: so-called Blue HotDOGs with a blue/UV excess observed with SDSS photometry. Although we cannot ascertain the origin of the blue slope with the current *Gemini*/GNIRS data, scattered light is a promising possibility and would strengthen the case that these sources are indeed obscured quasars. The discovery of these blue-slope sources and other obscured quasar candidates reveals that the population of obscured quasars has diverse properties. Also, these detections show that caution is needed when applying strict UV/optical dropout requirements to identify obscured quasars, further supporting our hypothesis that obscured quasars are simply missed. Using physically motivated, strategic colour-selections, such as ours, can uncover the diverse populations of obscured quasars.

4.4 Comparing/linking with other obscured quasars

As discussed earlier, the colours of our targets overlap with other types of obscured quasars. However, we see some key spectral differences, which may probe different physics. Perhaps we are probing the transitional link between the two populations. Assef et al. (2022) provided a physical model suggesting that the transitional link between HotDOGs, BHDs, and ERQs may be the interaction between the quasar-driven outflow and the obscuring medium. In this model, (1) the central quasar of HotDOGs is completely enshrouded by the obscuring material; (2) then massive, fast-moving outflows pierce through and 'blow out' the obscuration as observed with ERQs (and possibly BHDs); and (3) finally, the column density of the obscuration is lowered, which is observed as heavily reddened Type-1 quasars.

In the standard unification model of active nuclei, we expect the kinematics of [O III] to be similar in obscured and unobscured sources, since this line is produced on extended scales and reflects the kinematics of the gas in the host galaxy (or at least not in the sphere of influence of the black hole due to its low critical density). Indeed, Temple et al. (2019) find that there are no statistical differences in the [O III] kinematics between obscured and unobscured quasars. One exceptional population of obscured quasars is ERQs, which show

extremely high widths of [O III], unmatched by any other quasar population (Zakamska et al. 2016; Perrotta et al. 2019). Our sample shows a broad range of [O III] velocities, similar to those of typical powerful quasars and somewhat below those in ERQs, as seen in Figs 4 and 5. We do find three sources (J0024−0012, J0215+0042, and J2334+0031) reaching ERQ-like velocities and IR luminosities, as shown in Fig. 5.

Here, we suggest that the transitional link may be observed in the [O III] luminosity and velocity versus $L_{5\mu m}$ space, as shown in Figs 4 and 5. An interesting observation is that the ERQ selection requires a high [C IV] equivalent width (Hamann et al. 2017), which may preferentially select reddened quasars with extreme [O III] emission and winds. Our [O III] emission lines (luminosity and kinematics) are nearly ×10 weaker than those seen in ERQs, yet likely significantly larger than HotDOGs. Since our targets show weak [O III], it is difficult to determine if winds are present, although they are unlikely to have extreme winds like ERQs. According to the Assef et al. (2022) model, our selections may identify sources in the transition between stage (1), appearing bluer than HotDOGs, and stage (2), appearing redder than ERQs with weaker [O III]. By adjusting the detection criteria of optical and IR emission and nuclear line kinematics criteria, we may be able to recover more obscured populations.

If our targets are indeed obscured quasars, then a literature review for spectral data on our broader samples of 373 objects suggests that the number density of obscured quasars is between 0.17 and 0.93 deg^2. This density is potentially comparable to the confirmed unobscured density to the same depth in W4 but does not exceed the unobscured number density. A conservative interpretation is that unobscured quasars may only outnumber obscured quasars by a small factor. However, there is a caveat that this selection is biased towards bright $W4 < 8$ Vega mag sources, which may fail to identify fainter quasars. Although more comprehensive studies are necessary to resolve the number density estimates, our spectroscopic confirmation of these targets as obscured quasars support our hypothesis that obscured quasars have been missed by previous studies.

5 CONCLUSIONS

The census of obscured quasars at high redshift remains incomplete. We present *Gemini*/GNIRS spectra of 24 luminous, red quasar candidates at $z \sim 2$ selected using *WISE*/W4 photometry from the SDSS Stripe 82 field. These sources have little to no detectable optical flux, yet have high *WISE*/W4 fluxes (W4 ≥ 5 mJy). This selection aims to probe the peak of the quasar-heated dust emission at rest frame $\sim$ 10µm while requiring high optical obscuration with SDSS dropouts. The use of the *Spitzer* data ensures precise astrometry for these optically faint sources. This study probes a slightly different, yet complementary selection regime compared to that of other known red, obscured quasars like HotDOGs and ERQs.

From spectroscopic analysis, we find a diverse range of spectral types. Two sources show strong continuum and strong emission lines, six show moderate continuum and emission lines, and others show no continuum with weak emission lines if detected. All sources with continuum detection have a red slope. We detect moderately strong Hα and [O III] emission lines, which we use to determine the redshift of these sources. We find that our *WISE*-selected IR bright colour-selection method selects $1 < z < 3$ objects with the average redshift of $\langle z_{\text{best}} \rangle = 2.008 \pm 0.45$. Due to the low SNR of the emission lines detected, we fit single Gaussians to the continuum-subtracted spectra and we cannot study the details of line kinematics. From these fits, we find broad Hα emission lines

with FWHM ranging several 10^3 km s^{-1} and luminosities reaching 10^{42}–$10^{43.4}$erg s^{-1}. Very little Hβ is detected, whereas the [O III] doublet show clear detections. [O III]λ5009Å show moderate line strengths with luminosities 10^{42}–10^{43}erg s^{-1} and FWHM of several 10^3 km s^{-1}. The red slope and the lack of Hβ detections with large Hα/Hβ ratios are indicative that these sources are experiencing significant extinction with $\langle A_V(H\alpha/H\beta) \rangle \sim 4.8 \pm 2.8$ mag. We estimate the A_V extinction from the SED to probe the origin of the observed obscuration. We find typical values of $A_{V,\text{SED}} \sim 7$–20. The SED modelling indicate that these are indeed obscured quasars with a heavily reddened quasar+torus-dominated spectrum.

As expected from the large *WISE*/W4 fluxes, we find that these sources have large L_{bol} reaching $\sim 10^{46}$–10^{47}erg s^{-1}, which is comparable to some of the brightest known quasars. Compared to known unobscured and obscured quasars at the similar redshift and L_{bol}, we find that the [O III] line widths of our sources are similar to Type-1 quasars. Our sources do not display any signs of powerful quasar-driven winds such as those seen in ERQs (Zakamska et al. 2016; Perrotta et al. 2019). This suggests that the 'red-ness' of the quasar does not necessarily ensure the presence of strong winds.

The population of quasars we have discovered and characterized in this paper appears to be an intermediate one between HotDOGs and ERQs, with HotDOGs likely the most obscured. The differences in the properties are apparent from the shapes of the optical-to-IR SED and from the relative strengths of the emission lines. The red quasars of Temple et al. (2019) are significantly less obscured. It would be interesting to determine whether the column densities of X-ray absorbing gas in comparison to those of ERQs (Goulding et al. 2018) and HotDOGs (Vito et al. 2018) support this picture.

---

[1]https://pypeit.readthedocs.io/en/latest/
[2]http://www.astropy.org

DATA AVAILABILITY

Gemini data are publicly available from the Gemini Observatory Archive (GOA) located at https://archive.gemini.edu under GN-2017B-Q-51 (PI: Richards). WISE data are accessible by the Infrared Science Archive (IRSA) at https://irsa.ipac.caltech.edu/Missions/wise.html.

REFERENCES

Alexandroff R. M. et al., 2018, MNRAS, 479, 4936
Antonucci R., 1993, ARA&A, 31, 473
Assef R. J. et al., 2015, ApJ, 804, 27
Assef R. J. et al., 2016, ApJ, 819, 111
Assef R. J. et al., 2022, ApJ, 934, 101
Astropy Collaboration et al., 2022, ApJ, 935, 167
Banerji M., Alaghband-Zadeh S., Hewett P. C., McMahon R. G., 2015, MNRAS, 447, 3368
Bischetti M. et al., 2017, A&A, 598, A122
Brand K. et al., 2007, ApJ, 663, 204
Calzetti D., Armus L., Bohlin R. C., Kinney A. L., Koornneef J., Storchi-Bergmann T., 2000, ApJ, 533, 682
Canalizo G., Stockton A., 2001, ApJ, 555, 719
Cardelli J. A., Clayton G. C., Mathis J. S., 1989, ApJ, 345, 245
Dey A. et al., 2008, ApJ, 677, 943
Donley J. L. et al., 2012, ApJ, 748, 142
Dopita M. A., Sutherland R. S., 2003, Astrophysics of the diffuse universe. Springer, Berlin
Eisenhardt P. R. M. et al., 2012, ApJ, 755, 173
Elias J. H., Rodgers B., Joyce R. R., Lazo M., Doppmann G., Winge C., Rodríguez-Ardila A., 2006a, in McLean I. S., Iye M.eds, SPIE Conf. Ser. Vol. 6269, SPIE Astronomical Telescopes + Instrumentation. SPIE, Bellingham, p. 626914
Elias J. H., Joyce R. R., Liang M., Muller G. P., Hileman E. A., George J. R., 2006b, in McLean I. S., Iye M.eds, SPIE Conf. Ser. Vol. 6269, SPIE Astronomical Telescopes + Instrumentation. SPIE, Bellingham, p. 62694C
Elitzur M., Shlosman I., 2006, ApJ, 648, L101
Glikman E. et al., 2012, ApJ, 757, 51
Glikman E. et al., 2013, ApJ, 778, 127
Glikman E. et al., 2018, ApJ, 861, 37
Gordon K. D., Clayton G. C., Misselt K. A., Landolt A. U., Wolff M. J., 2003, ApJ, 594, 279
Goulding A. D. et al., 2018, ApJ, 856, 4
Greene J. E., Ho L. C., 2005, ApJ, 630, 122
Hamann F. et al., 2017, MNRAS, 464, 3431
Harrison C. M. et al., 2012, MNRAS, 426, 1073
Hasinger G., 2008, A&A, 490, 905
Hennawi J. F., Prochaska J. X., 2013, ApJ, 766, 58
Hickox R. C., Alexander D. M., 2018, ARA&A, 56, 625
Hopkins P. F., Hernquist L., Cox T. J., Di Matteo T., Robertson B., Springel V., 2006, ApJS, 163, 1
Ishikawa Y., Goulding A. D., Zakamska N. L., Hamann F., Vayner A., Veilleux S., Wylezalek D., 2021, MNRAS, 502, 3769
Jun H. D. et al., 2020, ApJ, 888, 110
Kennicutt Robert C. J., 1992, ApJ, 388, 310
Kim M., Ho L. C., Im M., 2006, ApJ, 642, 702
Konigl A., Kartje J. F., 1994, ApJ, 434, 446
Krolik J. H., Begelman M. C., 1988, ApJ, 329, 702
LaMassa S. M. et al., 2015, ApJ, 800, 144
LaMassa S. M., Yaqoob T., Boorman P. G., Tzanavaris P., Levenson N. A., Gandhi P., Ptak A. F., Heckman T. M., 2019, ApJ, 887, 173
Lacy M. et al., 2004, ApJS, 154, 166
Lacy M. et al., 2013, ApJS, 208, 24
Lanzuisi G., Piconcelli E., Fiore F., Feruglio C., Vignali C., Salvato M., Gruppioni C., 2009, A&A, 498, 67
Lawrence A., 1991, MNRAS, 252, 586
Lawrence A., Elvis M., 2010, ApJ, 714, 561
Liu G., Zakamska N. L., Greene J. E., Nesvadba N. P. H., Liu X., 2013, MNRAS, 436, 2576
Lonsdale C. J. et al., 2003, PASP, 115, 897
Lusso E. et al., 2013, ApJ, 777, 86
Mauduit J. C. et al., 2012, PASP, 124, 714
Osterbrock D. E., Ferland G. J., 2006, Astrophysics of gaseous nebulae and active galactic nuclei. University Science Books, Sausalito, CA
Papovich C. et al., 2016, ApJS, 224, 28
Perrotta S., Hamann F., Zakamska N. L., Alexandroff R. M., Rupke D., Wylezalek D., 2019, MNRAS, 488, 4126
Polletta M. et al., 2007, ApJ, 663, 81
Polletta M., Weedman D., Hönig S., Lonsdale C. J., Smith H. E., Houck J., 2008, ApJ, 675, 960
Prochaska J. X. et al., 2013, ApJ, 776, 136
Prochaska J. X. et al., 2020a, pypeit/PypeIt: Release 1.0.0
Prochaska J. X. et al., 2020b, J. Open Source Software, 5, 2308
Reyes R. et al., 2008, AJ, 136, 2373
Ricci C. et al., 2017, ApJ, 835, 105
Richards G. T. et al., 2006, AJ, 131, 2766
Riffel R. et al., 2021, MNRAS, 501, 4064
Ross N. P. et al., 2013, ApJ, 773, 14
Ross N. P. et al., 2015, MNRAS, 453, 3932
Sanders D. B., Soifer B. T., Elias J. H., Madore B. F., Matthews K., Neugebauer G., Scoville N. Z., 1988, ApJ, 325, 74
Sanders D. B. et al., 2007, ApJS, 172, 86
Shen Y., 2016, ApJ, 817, 55
Soltan A., 1982, MNRAS, 200, 115
Stern D. et al., 2005, ApJ, 631, 163
Temple M. J., Banerji M., Hewett P. C., Coatman L., Maddox N., Peroux C., 2019, MNRAS, 487, 2594
Timlin J. D. et al., 2016, ApJS, 225, 1
Treister E., Urry C. M., 2005, ApJ, 630, 115
Tsai C.-W. et al., 2015, ApJ, 805, 90
Ueda Y., Akiyama M., Ohta K., Miyaji T., 2003, ApJ, 598, 886
Vestergaard M., Peterson B. M., 2006, ApJ, 641, 689
Vito F. et al., 2018, MNRAS, 474, 4528
Werner M. W. et al., 2004, ApJS, 154, 1
Wright E. L. et al., 2010, AJ, 140, 1868
Wu J. et al., 2012, ApJ, 756, 96
Wu J. et al., 2018, ApJ, 852, 96
Yan L. et al., 2013, AJ, 145, 55
York D. G. et al., 2000, AJ, 120, 1579
Yu Q., Tremaine S., 2002, MNRAS, 335, 965
Yuan S., Strauss M. A., Zakamska N. L., 2016, MNRAS, 462, 1603
Zakamska N. L., Greene J. E., 2014, MNRAS, 442, 784
Zakamska N. L. et al., 2003, AJ, 126, 2125
Zakamska N. L. et al., 2006, AJ, 132, 1496
Zakamska N. L. et al., 2016, MNRAS, 459, 3144
Zakamska N. L. et al., 2019, MNRAS, 489, 497
Zappacosta L. et al., 2018, A&A, 618, A28

This paper has been typeset from a TEX/LATEX file prepared by the author.